nature COMMUNICATIONS

ARTICLE

Received 17 Sep 2016 | Accepted 10 Apr 2017 | Published 9 Jun 2017

DOI: 10.1038/ncomms15570 OPEN

Mesoscopic chaos mediated by Drude electron-hole plasma in silicon optomechanical oscillators

Jiagui Wu[1,2,*], Shu-Wei Huang[2,*], Yongjun Huang[2], Hao Zhou[2], Jinghui Yang[2], Jia-Ming Liu[3], Mingbin Yu[4], Guoqiang Lo[4], Dim-Lee Kwong[4], Shukai Duan[1] & Chee Wei Wong[2]

Chaos has revolutionized the field of nonlinear science and stimulated foundational studies from neural networks, extreme event statistics, to physics of electron transport. Recent studies in cavity optomechanics provide a new platform to uncover quintessential architectures of chaos generation and the underlying physics. Here, we report the generation of dynamical chaos in silicon-based monolithic optomechanical oscillators, enabled by the strong and coupled nonlinearities of two-photon absorption induced Drude electron–hole plasma. Deterministic chaotic oscillation is achieved, and statistical and entropic characterization quantifies the chaos complexity at 60 fJ intracavity energies. The correlation dimension D_2 is determined at 1.67 for the chaotic attractor, along with a maximal Lyapunov exponent rate of about 2.94 times the fundamental optomechanical oscillation for fast adjacent trajectory divergence. Nonlinear dynamical maps demonstrate the subharmonics, bifurcations and stable regimes, along with distinct transitional routes into chaos. This provides a CMOS-compatible and scalable architecture for understanding complex dynamics on the mesoscopic scale.

[1] College of Electronic and Information Engineering, Southwest University, Chongqing 400715, China. [2] Fang Lu Mesoscopic Optics and Quantum Electronics Laboratory, University of California, Los Angeles, California 90095, USA. [3] Electrical Engineering, University of California Los Angeles, California 90095, USA. [4] Institute of Microelectronics, A*STAR, Singapore 117865, Singapore. * These authors contributed equally to this work. Correspondence and requests for materials should be addressed to S.D. (email: duansk@swu.edu.cn) or to C.W.W. (email: cheewei.wong@ucla.edu).

Investigation of chaos and the associated nonlinear dynamics has spurred fundamental progress of science and technology. It brought new perspectives in a multitude of fields spanning from recurrent neural networks[1], relativistic billiards-like electron transport[2], fractal space and time[3] to self-organization in the natural sciences[4], amongst others. Chaos in optical systems has emerged and drawn much attention owing to its unique features and broad applications, including chaos-based synchronized secure optical communications[5–7], high-performance light detection and range finding[8] and ultrafast physical random bit generation[9]. Studies of chaos generation in III–V laser components have further shown progress in harnessing the broadband carriers in both the near infrared and the mid-infrared wavelength ranges[10–17], although the challenges of monolithic integration and circumventing the seemingly universal requirement of external perturbations remain to be solved.

Concurrently, significant efforts in nanofabrication technology and cavity optomechanics have led to the demonstration of regenerative oscillations in mesoscopic resonators[18–21]. Excited by centrifugal radiation pressure, optomechanical chaotic quivering was experimentally observed in toroidal whispering-gallery-mode microcavities[22]. Recently, in the toroidal whispering-gallery-mode microcavity, stochastic resonance and chaos have been transferred between two optical fields[23] with the chaotic physical basis through a strong nonlinear optical Kerr response from the nonlinear coupling of the optical and mechanical modes. This is complemented by recent theoretical studies on chaos including electro-optomechanical systems and potential routes into chaos[24,25].

Here, we couple the prior single optomechanical basis with a second basis—that of electron–hole plasma oscillations in the same cavity—to deterministically generate dynamical chaos in a silicon photonic crystal cavity. Differing from the prior studies, the silicon experimental platform enables electron–hole plasma dynamical generation, destabilizing the system dynamics and provides a route for chip-scale planar electronic–photonic integration. Our photonic crystal implementation is based on a slot-type optomechanical (OM) cavity with sub-wavelength [$\approx 0.051(\lambda/n_{air})^3$] modal volumes V, and high quality factor-to-volume ratios Q/V (refs 26,27). This provides strong optical gradient oscillation[26,28] to achieve operating intracavity energies of $\sim$60 fJ and enables near-single-mode operation. Our two-oscillator OM cavity is designed with comparable dynamical oscillation timescales between the Drude electron–hole plasma and radiation pressure optomechanics, which allows the chaotic attractors and unique trajectories to be uncovered. We present the statistical and entropic characteristics of the nonlinear dynamical regimes and illustrate the transition routes into and out of chaos. Our first-principles numerical modelling, including coupled oscillations in seemingly unrelated degrees of freedom (two-photon-induced free-carrier and thermal dynamics with radiation pressure dynamics) capture the experimental observations, the multi-period orbits and the trajectory divergence into chaotic states.

Results

Experimental observation of chaos. Figure 1a shows the scanning electron micrograph of the slot-type optomechanical photonic crystal cavity mediated by Drude electron–hole plasma investigated in this study. The air-bridged photonic crystal cavity is introduced with shifted-centre air holes that are shifted by 15, 10 and 5 nm, respectively, as shown in Fig. 1b. The width-modulated line-defect photonic crystal cavity design has a total quality factor Q of 54,300 (Fig. 1c) and a sub-wavelength modal volume of $0.051(\lambda/n_{air})^3$ (Fig. 1b inset) at the 1572.8 nm resonance wavelength (λ_o, with effective mode index n). The optomechanical cavity consists of two (16.0 μm × 5.5 μm × 250 nm) micromechanical photonic crystal slabs, separated by a 120 nm slot width across the photonic crystal line defect. The in-plane mechanical mode has a 112 MHz fundamental resonance and, when driven into the regenerative oscillation regime, has a narrow sub-15-Hz linewidth at ambient pressure and room temperature[29]. The large optical field gradient from the tight slot cavity photon confinement enables a large coherent optomechanical coupling strength, g_0, of $\sim$690 kHz (detailed in Supplementary Note 4), resulting in low-threshold optomechanical oscillation (OMO)[26–29]. Concurrently, on the same cavity, strong nonlinearities such as two-photon absorption (TPA), free-carrier and thermo-optic dynamical effects lead to modulation of the intracavity field[30]. Note the characteristic timescales of the OMO and the photonic crystal carrier dynamics are made comparable through our designed mechanical modes and intrinsic free-carrier diffusion times, enabling the coupled equations of motion to have sufficient overlap and degrees of freedom for chaos generation.

Figure 1d depicts the transition into chaos as the pump detuning to the cavity resonance Δ ($=\lambda_L-\lambda_0$, where λ_L is the injection light wavelength) is scanned from 0.2 to 4.2 nm with the injection power fixed at 1.26 mW detailed in Methods section). The chaos region as well as the associated dynamical transitional states can be identified. First, a stable pure fundamental OMO at 112 MHz is observed at the beginning of the detuning drive. With increased detuning, aperiodic and sub-oscillatory structures emerges when Δ is set in the range of 1.2–2.0 nm. Unstable pulses (USP) occur first, before the system is driven into a series of stable sub-harmonic pulse states such as the $f_{omo}/4$ states (oscillation period being four times the OMO period), the $f_{omo}/3$ states and the $f_{omo}/2$ states, respectively. For detuning Δ between 2.0 and 2.33 nm, the system exhibits a chaos region characterized by both a broadband radio frequency (RF) spectrum and an intricate phase portrait. For detuning $\Delta > 2.33$ nm, the system is driven to exit the chaos region by evolving into a $f_{omo}/2$ state ($\Delta = 2.33$–3.2 nm) before cumulating into a self-induced optical modulation (SOM) state ($\Delta = 3.2$–4.2 nm)[30,31]. Of note, the oscillation period of SOM ($\sim$13–17 ns), mainly determined by the Drude plasma effect and the thermal dissipation rate, is comparable with that of OMO ($\sim$9 ns). The close oscillation frequencies of SOM and OMO facilitate their effective interaction in the photonic crystal nanocavity and the occurrence of chaos[4,18].

Figure 2 shows an example chaotic oscillation in the temporal domain and its RF frequency spectrum with the recorded raw temporal waveform shown in Fig. 2a, illustrating the irregular and intricate fluctuations. Figure 2b presents the phase portrait of chaos in a two-dimensional plane spanned by the power of the temporal waveform (P, horizontal axis) and its first time derivative (σ, vertical axis)[32]. The reconstructed trajectory is useful for illustrating the complex geometrical and topological structure of the strange attractor, showing the local instability, yet global stable nature, of a chaos structure[32]. To reveal the topological structure of chaos attractors, a state-space procedure is implemented to average the temporal waveform points in an m-dimensional embedded space[32] (detailed in Supplementary Note 1) by removing stochastic noise from the recorded raw data. The noise removal enables a clear depiction of the topological structure of the attractor and is also useful for the estimation of correlation dimension and Kolmogorov entropy, the most commonly used measures of the strangeness of chaotic attractors and the randomness of chaos[33–36]. Furthermore, Fig. 2c shows the corresponding RF spectrum, where the signal distributes broadly and extends up to the cutoff frequency of the

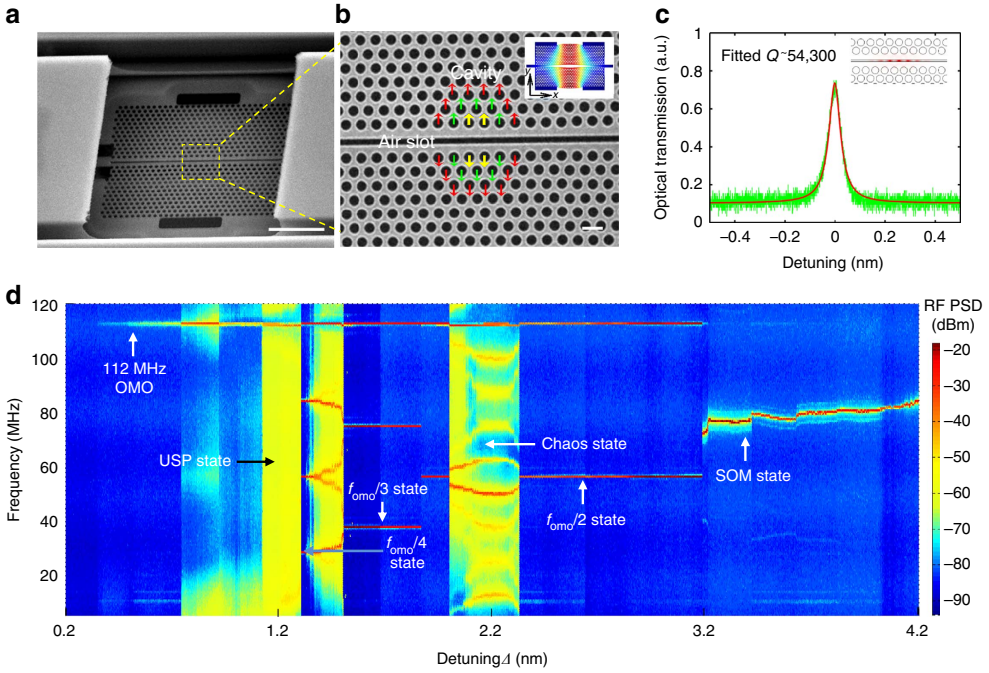

Figure 1 | Observations of dynamical chaos in mesoscopic optomechanical cavities. (**a**) Scanning electron micrograph of the optomechanical cavity. Scale bar, 5 μm. (**b**) Zoom-in of 120 nm slot cavity with localized resonant mode formed by perturbed neighbouring holes at the cavity centre, with amplitude displacements denoted by the coloured arrows (yellow: 15 nm; green: 10 nm; and red: 5 nm). The lattice constant is 500 nm and the ratio between hole radius and lattice constant is 0.34. Scale bar, 500 nm. Inset: finite-element model of the fundamental mechanical mode field, with normalized displacement magnitude shown in colour (red as maximum displacement and blue as zero displacement). (**c**) Measured optical transmission spectrum with a cold cavity loaded quality factor Q of 54,300 under low injection power and centred at 1572.8 nm. Inset: $|E|^2$ field distribution of the fundamental optical resonance, with normalized intensity magnitude shown in colour (red as maximum intensity and white as zero intensity). (**d**) 2D RF spectral map illustrating the evolution of nonlinear and chaotic dynamics, detailed as OMO (OMO) state - USP state-f_{omo}/4 state-f_{omo}/3 state-chaos state-f_{omo}/2 state-SOM state, under controlled laser-cavity detuning Δ and at 1.26 mW injection power.

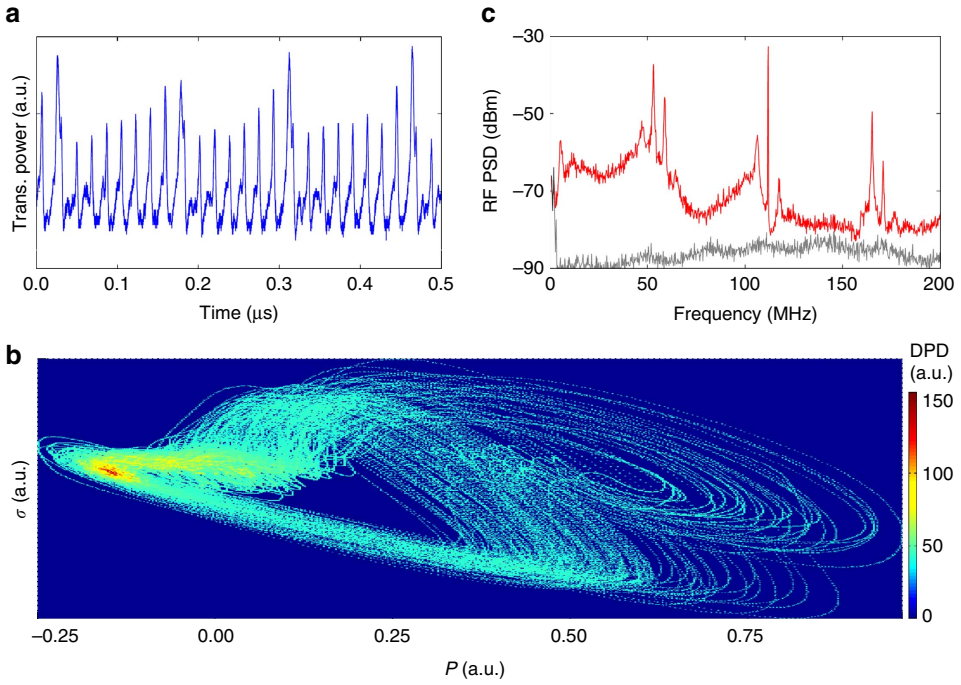

Figure 2 | Frequency-time characterization of the chaos. (**a**) Raw temporal waveform of chaotic output. (**b**) Corresponding phase portraits of the noise-reduced temporal waveform, where the colour evolution from cyan to orange to red is proportional to the data point density (DPD) in the measured temporal orbit. (**c**) Corresponding measured RF power spectral density (PSD). The grey curve is the reference background noise floor.

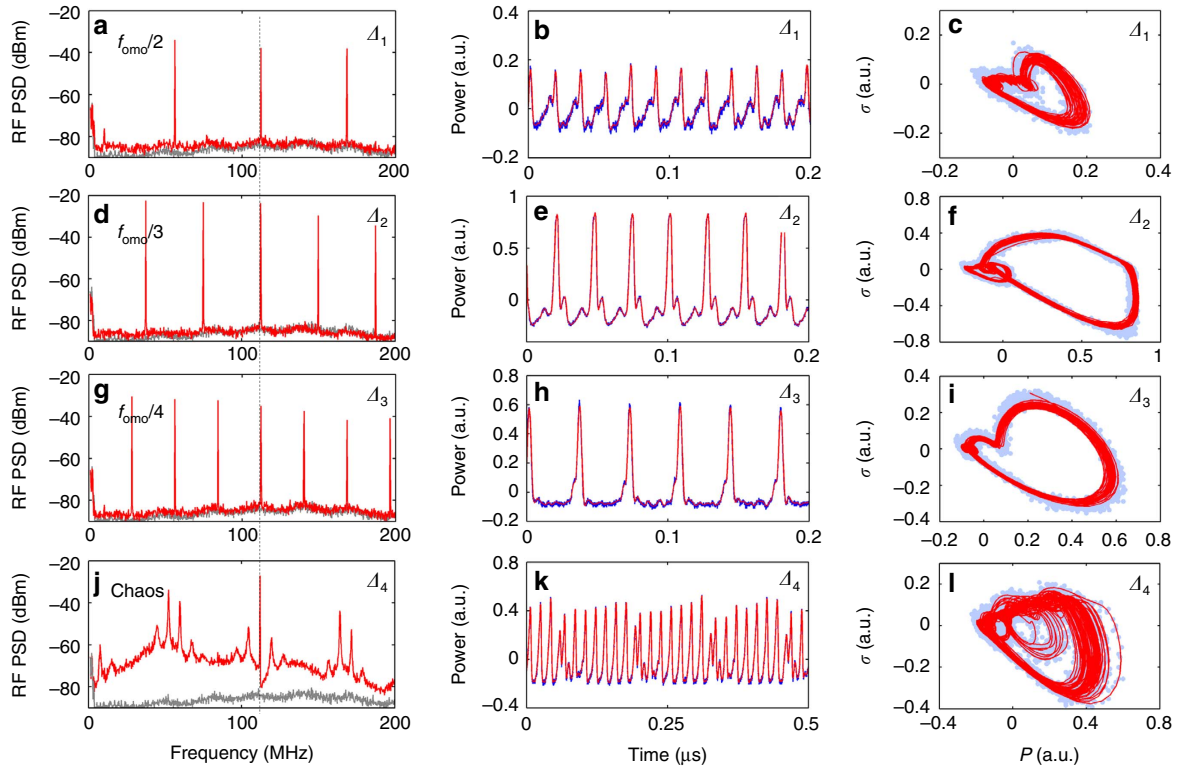

Figure 3 | Dynamical states under controlled drive conditions. (**a**–**c**) the $f_{omo}/2$ state ($\Delta_1 \approx 2.406$ nm), (**d**–**f**) the $f_{omo}/3$ state ($\Delta_2 \approx 1.831$ nm), (**g**–**i**) the $f_{omo}/4$ state ($\Delta_3 \approx 1.394$ nm) and (**j**–**l**) the chaos state ($\Delta_4 \approx 2.285$ nm) respectively. The curves (**a**,**d**,**g**,**j**) are the measured RF power spectral density (PSD) where the grey curves are the background noise floor. Notice the subharmonics have the background at the noise floor. The curves (**b**,**c**,**e**,**f**,**h**,**i**,**k**,**l**) are the temporal waveforms and orbital phase portraits, where the blue dots are the measured raw data and the solid red curves are the noise-reduced orbital trajectories.

measurement instrumentation, showing a hallmark spectral feature of chaos.

Figure 3 illustrates the detailed properties of several different dynamical states, including RF spectra, temporal waveforms and phase portraits. First, Fig. 3a shows the frequency and temporal characteristics of the $f_{omo}/2$ state. We observe three characteristic features of the $f_{omo}/2$ state:distinct $f_{omo}/2$ components in the RF spectrum (Fig. 3a), pulses with period ($\approx$17.8 ns) at two times the OMO period ($\approx$8.9 ns) in the temporal waveform (Fig. 3b), and clear limit cycle[37] features in the phase portrait (Fig. 3c). Similarly, Fig. 3d–f,g–i show the frequency spectra, the temporal waveforms at a third and a quarter of the fundamental oscillation, and the corresponding limit cycle phase portraits of the transitional $f_{omo}/3$ and $f_{omo}/4$ states, respectively. We note the satellite bumps next to the main peaks in the temporal waveforms; they represent the relatively weak OMO fundamental oscillations. Figure 3j,k next show the frequency and temporal features of the chaos state, where a broadband spectrum and a fluctuating temporal waveform are observed. In the phase portrait (Fig. 3l), the trajectory evolves intricately and scatters widely in phase space, being quite different from other periodical dynamics. With this slot cavity and at 1.26 mW injection power ($\sim$60 fJ intracavity energy), the specific transition route is OMO-USP-$f_{omo}/4$-$f_{omo}/3$-$f_{omo}/2$-chaos-$f_{omo}/2$-SOM, exhibiting a clear sub-harmonic route to chaos. The complete set of routing states into/out of chaos is detailed in Supplementary Note 2.

Dynamical characterization of chaos. Next, statistical analysis is performed to uncover the detailed dynamical properties of the chaotic states. A three-dimensional phase space is constructed in Fig. 4a, in a volumetric space spanned by the power (P), the first time derivative of P (σ) and the second time derivative of P (ξ). The green curves are the projections of the trajectory onto each of the three phase planes, showing the geometric structures. Three statistical measures, Lyapunov exponents (LEs), correlation dimension and Kolmogorov entropy, are commonly employed to illustrate and characterize the dynamical properties of chaos[32–38]. Details of these measures are provided in Supplementary Note 1. LEs, which describe the divergence rate of nearby attractor trajectories, are the most widely employed criteria in defining chaos[33]. In Fig. 4b, we show the calculated LEs, converging to values $\lambda_1 \approx 0.329$, $\lambda_2 \approx -0.087$ and $\lambda_3 \approx -0.946\,\mathrm{ns}^{-1}$ respectively, or equivalently, when expressed on the intrinsic optomechanical photonic crystal cavity, timescale ($\tau_{omo} = f_{omo}^{-1} \approx 8.9$ ns) $\lambda_1 \approx 2.94\tau_{omo}^{-1}$, $\lambda_2 \approx -0.78\tau_{omo}^{-1}$ and $\lambda_3 \approx -8.45\tau_{omo}^{-1}$. The maximal LE is positive, illustrating a fast divergence rate between adjacent orbits and indicating that the system is chaotic[32,33]. We further analyse the correlation dimension D_2:

$$D_2 = \lim_{\substack{D\to\infty \\ r\to 0}} \frac{d\ln(C_D(r))}{d\ln(r)} \qquad (1)$$

where C_D is the correlation integral of vector size D in an r radius sphere and d is the Euclidian norm distance[36]. A conservative estimate of the attractor correlation dimension is implemented through the Grassberger-Procaccia algorithm[36,38] as detailed in Supplementary Note 1. As shown in Fig. 4c, the correlation integrals C_D vary with sphere radius r. In Fig. 4d, the plot of the correlation integral slope versus sphere radius r is obtained by

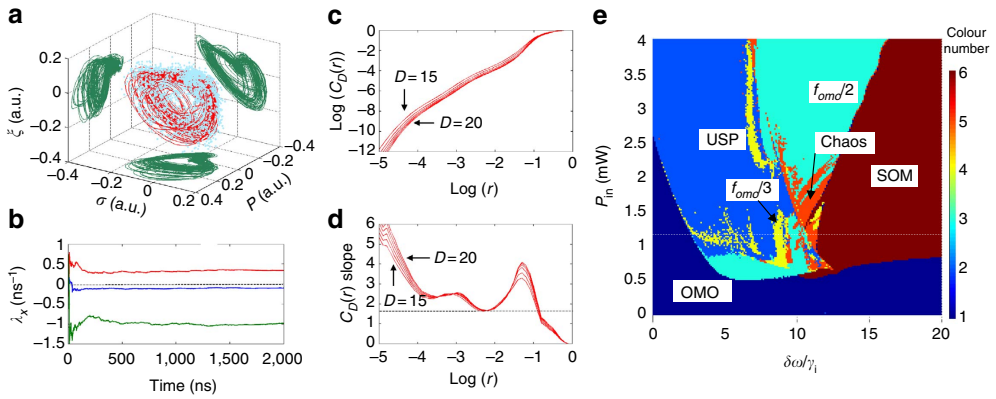

Figure 4 | Chaos identification and regime distribution map. (**a**) Measured three-dimensional portrait in phase space. The blue dots are the measured raw data, while the solid red curve is the reconstructed trajectory. The three green phase portraits are projections of the 3D portrait onto the phase planes. (**b**) Calculated LEs spectrum. The curves converge to the LE values as $\lambda_1 \approx 0.329$, $\lambda_2 \approx -0.087$ and $\lambda_3 \approx -0.946\,\mathrm{ns}^{-1}$. (**c**) Logarithmic plots of the correlation integral $C_D(r)$ versus sphere radius r based on the Grassberger-Procaccia algorithm. (**d**) Slope of the correlation integral versus sphere radius r. A clear plateau on the slope of the correlation integral is observed and marked with the horizontal dashed line. The correlation dimension D_2 is estimated at ≈ 1.67. In **c**,**d**, the lines denote the vector size D from 15 to 20 in integer steps. (**e**) Dynamical distribution map based on the numerical modelling. Different colours denote different dynamical states, including OMO (OMO, dark blue) state, USP (light blue) state, $f_{omo}/3$ state (yellow), $f_{omo}/2$ state (cyan), chaos state (orange) and SOM (SOM, dark red) state. The OMO state, USP state, $f_{omo}/3$ state and $f_{omo}/2$ state denote the periodic and low-entropy dynamical regimes; the chaos state and SOM state denote the high-entropy dynamical regimes. The horizontal axis is the normalized laser-cavity detuning $\delta\omega/\gamma_i$ and the vertical axis is the injected optical power P_{in}. The dashed white horizontal line is an example corresponding to the injected power level in the measurement.

extracting the slope from Fig. 4c. A clear plateau of the correlation integral slope is observed, supporting the estimated value of D_2 at ~ 1.67 ($D_2 \approx 2.0$ without noise filtering). The correlation dimension D_2 highlights the fractal dimensionality of the attractor and demonstrates the strangeness of the complex geometrical structure[34]. We note that this D_2 value is already higher than that of several canonical chaos structures such as the Hénon map (at 1.21), the logistic map (at 0.5), and the Kaplan-Yorke map (at 1.42), and is even close to that of Lorenz chaos (at 2.05)[36].

Furthermore the waveform unpredictability can be characterized by the second-order Renyi approximation of the Kolmogorov entropy K_2:

$$K_2 = \lim_{\substack{D\to\infty \\ r\to 0}} \frac{1}{\tau} \ln\left(\frac{C_D(r)}{C_{D+1}(r)}\right) \tag{2}$$

where τ is the time series sampling rate, a measurement of the system uncertainty and a sufficient condition for chaos[38]. A positive K_2 is characteristic of a chaotic system, while a completely ordered system and a totally random system will have $K_2 = 0$ and $K_2 = \infty$ respectively. With the Grassberger-Procaccia algorithm, K_2 is calculated as $\approx 0.17\,\mathrm{ns}^{-1}$ or expressed equivalently as $\approx 1.52\tau_{omo}^{-1}$, representing that the mean divergence rate of the orbit section (with adjoining point pairs in the phase space) is rapid within 1.52 times the fundamental OMO period. It characterizes the gross expansion of the original adjacent states on the attractor[38] and, therefore, indicates the significant unpredictability in the dynamical process of such solid-state systems.

Theoretical simulation of chaos. To further support the physical observations, we model the dynamics of the optomechanical photonic crystal cavity system under the time-domain nonlinear coupled mode formalism, taking into account the OMO[21], TPA[31], free-carrier and thermo-optic dynamics[30,31]:

$$\frac{d^2x}{dt^2} + \Gamma_m \frac{dx}{dt} + \Omega_m^2 x(t) = \frac{g_0}{\omega_0}\sqrt{\frac{2\Omega_m}{\hbar m_{eff}}}|A(t)|^2 \tag{3}$$

$$\frac{dA}{dt} = i\left(-g_0\sqrt{\frac{2m_{eff}\Omega_m}{\hbar}}x(t) + \frac{\omega_0}{n_{Si}}\left(\frac{dn_{Si}}{dT}\Delta T(t) + \frac{dn_{Si}}{dN}N(t)\right) + \delta\omega\right)A(t) - \frac{1}{2}\left(\gamma_i + \gamma_e + \frac{\Gamma_{TPA}\beta_{Si}c^2}{V_{TPA}n_g^2}|A(t)|^2 + \frac{\sigma_{Si}cN(t)}{n_g}\right)A(t) + \sqrt{\gamma_e P_{in}} \tag{4}$$

$$\frac{dN}{dt} = -\frac{N(t)}{\tau_{fc}} + \frac{\Gamma_{FCA}\beta_{Si}c^2}{2\hbar\omega_0 n_g^2 V_{FCA}^2}|A(t)|^4 \tag{5}$$

$$\frac{d\Delta T}{dt} = -\frac{\Delta T(t)}{\tau_{th}} + \frac{\Gamma_{PhC}}{\rho_{Si}c_p V_{PhC}}\left(\gamma_i + \frac{\Gamma_{TPA}\beta_{Si}c^2}{V_{TPA}n_g^2}|A(t)|^2 + \frac{\sigma_{Si}cN(t)}{n_g}\right)|A(t)|^2 \tag{6}$$

where x, A, N and ΔT represent respectively the motional displacement, the intracavity **E**-field amplitude, the free-carrier density and the cavity temperature variation. $\delta\omega = \omega_L - \omega_0$ is the detuning between injection light, ω_L, and photonic crystal cavity resonance, ω_0, and P_{in} is the injected optical power (detailed in Supplementary Note 3, Supplementary Table 1). Equation (3) describes the optically driven damped mechanical harmonic oscillation with self-sustained OMO oscillations when pumped above threshold. The mechanical oscillations then in turn result in modulation of the intracavity optical field (first term on the right-hand side of equation (4)). On the other hand, the plasma induced thermal-optic effect and free-carrier dispersion in the cavity (second and third terms on the right-hand side of equation (4)) lead to another amplitude modulation of the intracavity field. Here, the high-density Drude plasma is generated by the strong TPA in silicon (equation (5)). With the increased intracavity power, the free-carrier dispersion effect leads to blue-shifts of the cavity resonance while the free-carrier

absorption induced thermo-optic effect results in red-shifts of the cavity resonance. The dynamical interplay between these two effects results in the regenerative SOM (refs 30,31). The mechanism is detailed in Supplementary Fig. 6 and Supplementary Note 6. We note that our photonic crystal design ensures that the characteristic timescales of the SOM and OMO oscillations are on the same order of magnitude (Supplementary Fig. 8), strengthening the effective inter-oscillator coupling. The coexistence of OMO and SOM mechanisms adds extra degrees of freedom to the dynamic space of system and results in increased susceptibility to destabilization (detailed in Supplementary Note 2)[16,18,21].When the drive power is between the SOM and OMO thresholds, TPA-associated amplitude modulations disrupt the OMO rhythm, breaking the closed OMO limit cycles and creating the non-repeating chaotic oscillations. On the other hand, if the frequency ratio between OMO and SOM is close to a rational value, they will lock each other based on the harmonic frequency locking phenomena[39,40]. Consequently, different sub-harmonic f_{omo} states are also observed in Fig. 3. Effects of the Drude free-carrier plasma, the detuning $\delta\omega$, the optomechanical coupling strength g_0 and the injected drive power P_{in} on the chaotic transitions and routes are detailed in Supplementary Notes 4–7.

Figure 4e shows the dynamical distribution map simulated numerically and parametrically with the normalized detuning $\delta\omega/\gamma_i$ versus injection power P_{in}, where γ_i is the intrinsic cavity linewidth from linear losses. The various regimes are denoted with different colours, and rigorously identified through entropic analysis of the temporal waveform uncertainty and periodicity of the Fourier spectrum. The temporal waveforms are often strongly periodic in the limit cycle states (such as OMO and USP) and have low entropy (indicated by the darker colours), while the chaotic oscillation has a significant uncertainty and high entropy (indicated by the brighter colours). In Fig. 4e, the crescent-shaped region (in bright orange) indicates the parametric conditions of the complex chaos state. Around this region, there are rich transitional dynamics related to chaos, thereby enabling different routes into or out of chaos with different parameter scanning approaches. When the pump power is 1.26 mW, the numerical model predicts a bifurcation transition to chaos via states OMO-USP-f_{omo}/3-f_{omo}/2-chaos-SOM as a function of detuning, in a qualitative agreement with the experimental observations. It is of note that the system of coupled equations does not involve any initial noise terms, illustrating the deterministic nature of the obtained chaotic solutions.

Discussion

We demonstrate chaos generation in mesoscopic silicon optomechanics achieved through single-cavity coupled oscillations between radiation-pressure- and two-photon-induced free-carrier dynamics. Chaos generation is observed at 60 fJ intracavity energies, with a correlation dimension D_2 determined at $\sim$1.67. The maximal LE rate is measured at 2.94 times the fundamental OMO, and the second-order Renyi estimate of the Kolmogorov entropy K_2 is determined at 1.9 times the fundamental OMO, both showing fast adjacent trajectory divergence into the chaotic states. Furthermore, we route the chaos through unstable states and fractional subharmonics, tuned deterministically through the drive-laser detuning and intracavity energies. These observations set the path towards synchronized mesoscopic chaos generators for science of nonlinear dynamics and potential applications in secure and sensing application, in light of recent works about gigahertz OMOs[41] and synchronization of coupled optomechanical oscillators[42].

Methods

Device design and fabrication. The optomechanical photonic crystal cavity is fabricated with a CMOS-compatible process on 8-inch silicon wafers at the foundry, using 248 nm deep-ultraviolet lithography and reactive ion etching on 250 nm thickness silicon-on-insulator wafers. To realize the critical 120 nm slot width, the resist profile is patterned with a 185 nm slot linewidth, then transferred into a sloped oxide etch. The resulting bottom 120 nm oxide gap is etched into the silicon device layer through tight process control. Multiple planarization steps enable high-yield of the multi-step optomechanical photonic crystal fabrication. The optical input/output couplers are realized with silicon inverse tapers and oxide overcladding coupler waveguides. The optomechanical photonic crystal cavities are released by timed buffered oxide etch of the undercladding oxide.

Measurement set-up. The drive laser is a tunable Santec TSL-510C laser (1,510–1,630 nm), which is also used to measure the optical transmission spectra. The drive laser is first amplified by a C-band erbium-doped fibre amplifier and then injected into the slot-type photonic crystal cavity with a coupling lens placed on an adjustable 25-nm precision stage. A—fibre polarization controller with a prism polarizer selects the transverse-electric polarization state for the cavity mode. The output transmission of the photonic crystal cavity is collected into fibre through a coupling lens, an optical isolator, and then into a New Focus (Model 1811) detector, before an electronic spectrum analyzer (Agilent N9000A) and time-domain digital oscilloscope (Tektronix TDS 7404) characterization and statistical analysis.

Numerical simulations. The coupled equations (1)–(4) are numerically solved with the fourth-order Runge-Kutta algorithm. The time discretization is set as 10 ps and each simulated temporal waveform contains 10^7 data points (100 μs). The simulated RF spectrum is calculated with the fast Fourier transform method, which is a discrete Fourier transform algorithm to rapidly convert a signal from its time domain to a representation in the frequency domain. In frequency domain, we can easily get the spectral characteristics of the signal. The long time span of the temporal waveform (at 100 μs) is also necessary for resolving the 25 kHz spectral features and converging in the subsequent statistical analyses.

Data availability. The authors declare that the data supporting the findings of this study are available within the paper and its Supplementary Information files.

References

1. Laje, R. & Buonomano, D. V. Robust timing and motor patterns by taming chaos in recurrent neural networks. *Nat. Neurosci.* **16,** 925–933 (2013).
2. Ponomarenko, L. A. *et al.* Chaotic Dirac billiard in graphene quantum dots. *Science* **320,** 356–358 (2008).
3. Shlesinger, M. F., Zaslavsky, G. M. & Klafter, J. Strange kinetics. *Nature* **363,** 31–37 (1993).
4. Sornette, D. *Critical Phenomena In Natural Sciences: Chaos, Fractals, Self-Organization And Disorder: Concepts And Tools* (Springer, 2006).
5. Vanwiggeren, G. D. & Roy, R. Communication with chaotic lasers. *Science* **279,** 1198–1200 (1998).
6. Argyris, A. *et al.* Chaos-based communications at high bit rates using commercial fibre-optic links. *Nature* **438,** 343–346 (2005).
7. Virte, M., Panajotov, K., Thienpont, H. & Sciamanna, M. Deterministic polarization chaos from a laser diode. *Nat. Photon.* **7,** 60–65 (2013).
8. Lin, F.-Y. & Liu, J.-M. Chaotic lidar. *IEEE J. Sel. Top. Quantum Electron* **10,** 991–997 (2004).
9. Uchida, A. *et al.* Fast physical random bit generation with chaotic semiconductor lasers. *Nat. Photon.* **2,** 728–732 (2008).
10. Soriano, M. C., García-Ojalvo, J., Mirasso, C. R. & Fischer, I. Complex photonics: dynamics and applications of delay-coupled semiconductors lasers. *Rev. Mod. Phys.* **85,** 421–470 (2013).
11. Yousefi, M. *et al.* New role for nonlinear dynamics and chaos in integrated semiconductor laser technology. *Phys. Rev. Lett.* **98,** 044101 (2007).
12. Argyris, A., Hamacher, M., Chlouverakis, K., Bogris, A. & Syvridis, D. Photonic integrated device for chaos applications in communications. *Phys. Rev. Lett.* **100,** 194101 (2008).
13. Ohtsubo, J. *Semiconductor Lasers: Stability, Instability And Chaos* Vol. 111 (Springer Series in Optical Sciences, 2013).
14. Sciamanna, M. & Shore, K. A. Physics and applications of laser diode chaos. *Nat. Photon.* **9,** 151–162 (2015).
15. Wu, J. G., Xia, G. Q. & Wu, Z. M. Suppression of time delay signatures of chaotic output in a semiconductor laser with double optical feedback. *Opt. Express* **17,** 20124–20133 (2009).
16. Wu, J. G. *et al.* Direct generation of broadband chaos by a monolithic integrated semiconductor laser chip. *Opt. Express* **21,** 23358–23364 (2013).
17. Jumpertz, L., Schires, K., Carras, M., Sciamanna, M. & Grillot, F. Chaotic light at mid-infrared wavelength. *Light Sci. Appl.* **5,** e16088 (2016).

18. Arcizet, O., Cohadon, P.-F., Briant, T., Pinard, M. & Heidman, A. Radiation pressure cooling and optomechanical instability of a micromirror. *Nature* **444,** 71–74 (2006).
19. Thompson, J. D. *et al.* Strong dispersive coupling of a high-finesse cavity to a micromechanical membrane. *Nature* **452,** 72–75 (2008).
20. Kippenberg, T. J. & Vahala, K. J. Cavity optomechanics: back-action at the mesoscale. *Science* **321,** 1172–1176 (2008).
21. Aspelmeyer, M., Kippenberg, T. J. & Marquardt, F. Cavity optomechanics. *Rev. Mod. Phys.* **86,** 1391–1452 (2014).
22. Carmon, T., Cross, M. C. & Vahala, K. J. Chaotic quivering of micron-scaled on-chip resonators excited by centrifugal optical pressure. *Phys. Rev. Lett.* **98,** 167203 (2007).
23. Monifi, F. *et al.* Optomechanically induced stochastic resonance and chaos transfer between optical fields. *Nat. Photon.* **10,** 399–405 (2016).
24. Mei, W. *et al.* Controllable chaos in hybrid electro-optomechanical systems. *Sci. Rep.* **6,** 22705 (2016).
25. Bakemeier, L., Alvermann, A. & Fehske, H. Route to chaos in optomechanics. *Phys. Rev. Lett.* **114,** 013601 (2015).
26. Zheng, J. *et al.* Parametric optomechanical oscillations in two-dimensional slot-type high-Q photonic crystal cavities. *Appl. Phys. Lett.* **100,** 211908 (2012).
27. Noda, S., Chutinan, A. & Imada, M. Trapping and emission of photons by a single defect in a photonic band gap structure. *Nature* **407,** 608–610 (2000).
28. Safavi-Naeini, A. H., Alegre, T. P. M., Winger, M. & Painter, O. Optomechanics in an ultrahigh-Q two-dimensional photonic crystal cavity. *Appl. Phys. Lett.* **97,** 181106 (2010).
29. Luan, X. *et al.* An integrated low phase noise radiation-pressure-driven optomechanical oscillator chipset. *Sci. Rep.* **4,** 6842 (2014).
30. Yang, J. *et al.* Radio frequency regenerative oscillations in monolithic high-Q/V heterostructured photonic crystal cavities. *Appl. Phys. Lett.* **104,** 061104 (2014).
31. Johnson, T. J., Borselli, M. & Painter, O. Self-induced optical modulation of the transmission through a high-Q silicon microdisk resonator. *Opt. Express* **14,** 817–831 (2006).
32. Sprott, J. C. *Chaos and Time Series Analysis* (Oxford University Press, 2003).
33. Ott, E. *Chaos in Dynamical Systems* (Cambridge University Press, 2002).
34. Grassberger, P. & Procaccia, I. Measuring the strangeness of strange attractors. *Phys. D Nonlinear Phenom.* **9,** 189–208 (1983).
35. Schuster, H. G. *Deterministic Chaos: An Introduction* 3rd edn (Wiley, 1995).
36. Grassberger, P. & Procaccia, I. Characterization of strange attractors. *Phys. Rev. Lett.* **50,** 346–349 (1983).
37. Strogatz, S. H. *Nonlinear Dynamics And Chaos* (Addison-Wesley, 1994).
38. Grassberger, P. & Procaccia, I. Estimation of the Kolmogorov entropy from a chaotic signal. *Phys. Rev. A* **28,** 2591–2593 (1983).
39. Gilbert, T. & Gammon, R. Stable oscillations and Devil's staircase in the Van der Pol oscillator. *Int. J. Bifurcation Chaos* **10,** 155–164 (2000).
40. Lin, F. Y. & Liu, J. M. Harmonic frequency locking in a semiconductor laser with delayed negative optoelectronic feedback. *Appl. Phys. Lett.* **81,** 3128–3130 (2002).
41. Jiang, W. C., Lu, X., Zhang, J. & Lin, Q. High-frequency silicon optomechanical oscillator with an ultralow threshold. *Opt. Express* **20,** 15991–15996 (2012).
42. Zhang, M. *et al.* Synchronization of micromechanical oscillators using light. *Phys. Rev. Lett.* **109,** 233906 (2012).

Acknowledgements

We acknowledge discussions with Eli Kinigstein, Jing Dong, Jaime Gonzalo Flor Flores and Xingsheng Luan, and with Jiangjun Zheng on the initial design layout and measurements. This material is supported by the Office of Naval Research (N00014-14-1-0041), the China Postdoctoral Science Foundation (2017M612885), the Central Universities Funds of China (XDJK2017B038), and the Air Force Office of Scientific Research under award number FA9550-15-1-0081.

Author contributions

J.W., Y.H. and H.Z. performed the measurements, J.W., S.-W.H., J.Y. and C.W.W. performed the numerical simulations and design layout, M.Y., G.L. and D.-L.K. performed the device nanofabrication, and J.W., S.-W.H., J.-M.L., S.D. and C.W.W. discussed and put together the manuscript with contributions from all authors.

Additional information

Supplementary Information accompanies this paper at http://www.nature.com/naturecommunications

Competing interests: The authors declare no competing financial interests.

Reprints and permission information is available online at http://npg.nature.com/reprintsandpermissions/

How to cite this article: Wu, J. *et al.* Mesoscopic chaos mediated by Drude electron-hole plasma in silicon optomechanical oscillators. *Nat. Commun.* **8**, 15570 doi: 10.1038/ncomms15570 (2017).

Publisher's note: Springer Nature remains neutral with regard to jurisdictional claims in published maps and institutional affiliations.

Supplementary Note 1: Experimental data and chaos identification

In this section we analyze the experimentally recorded temporal waveforms. There are various kinds of noise processes in the experimental setup and measurements which can affect the process of chaos identification. Therefore it is necessary to reduce the noise in temporal waveforms. Here, the length of temporal waveforms is recorded over 10^5 data points with a high-sensitivity photodiode and a digital oscilloscope at 10 Gs/s sampling rate. We use the state-space averaging method to discriminate the stochastic noise from the chaotic waveform [1,2]. In this method, the *n*th data point of the recorded temporal waveforms is denoted by X_{n}. The noise-reduced data points are expressed as $\tilde{X}_n$. A sliding window is tied to X_{n} with a width $\pm m$ points in the state-space. Then, $\tilde{X}_n$ is expressed as [S1,S2]:

$$\tilde{X}_n = \frac{\sum_{k=m}^{N-m} X_k \omega_n(k)}{\sum_{k=m}^{N-m} \omega_n(k)}, \text{ and } \omega_n(k) = \exp(-\sum_{j=-m}^{m} (X_{k-j} - X_{n-j})^2 / \sigma_{noise}^2) \quad (1)$$

The data point $\tilde{X}_n$ averages the dataset X_{n} in a sliding $\pm m$ points window around X_{n} in the *m*-dimensional embedding space. $\omega_{\mathrm{n}}(k)$ gives the nearby points different weight; the nearer points have more weight. For our data, *m* is set as 10, σ_{noise} is the noise standard deviation and at 0.2 optimally, while maintaining the dynamical complexity of chaotic temporal waveform as shown in Figure 2b of the main text.

To identify the chaotic dynamics, we calculated the Lyapunov exponents (LEs) of the recorded time series. The LEs are critical measures of dynamical stability of a system. In mathematics, the LEs characterize quantitatively the rate of separation of infinitesimally close trajectories. Negative LEs are characteristic of dissipative stable systems. The more negative the LEs, the better the stability. Zero LE is characteristic of a conserved stable system. Positive LEs reveal the orbit is unstable and chaotic. Nearby points, no matter how close, will diverge to any arbitrary separation. Two trajectories in phase space with initial separation δZ_0 diverge (being treated with the linear approximation) at a rate given by [2]: $|\delta Z(t)| \approx e^{\lambda t} |\delta Z_0|$, where λ is the LE. In the multi-dimensional phase space, the rate of separation should be different for different orientations of the initial separation vector. Thus

there is a spectrum of Lyapunov exponents [3]. The largest of the LEs can be called the maximal Lyapunov exponent (MLE), and determines the notion of predictability for a dynamical system. A positive MLE is usually taken as an indication that the system is chaotic [2].

We next implement the canonical Grassberger-Procaccia (G-P) algorithm [4-6] to estimate the correlation dimension D_2 (close to the fractal dimension of attractor) and the K_2 entropy (close to the Kolmogorov entropy) [4-6]. For example, if we have a set of random points being distributed on a triangle face embedded in three-dimensional space or four-dimensional space, the correlation dimension will always be 2. The correlation dimension has the advantage of quick calculation, of only needing a small number of points, and often agreeing well with the results of other dimension estimation methods [6]. The convergence of the G-P algorithm is sufficient to demonstrate chaos and estimate its finite correlation dimension. During calculation, the value of D_2 could be calculated from the integral $C_D(r)$:

$$C_D(r) = \frac{1}{N^2}(\sum_{n,m}(d(X_n, X_m) < r)) \tag{2}$$

This formula is a numerical computation of the average number of vectors that could be found within a sphere of radius r around a given vector. Distance d is the Euclidian norm. From the analysis of Grassberger-Procaccia [4-6], we have:

$$D_2 = \lim_{\substack{D\to\infty \\ r\to 0}} \frac{d\ln(C_D(r))}{d\ln(r)} \quad \text{and} \quad K_2 = \lim_{\substack{D\to\infty \\ r\to 0}} \frac{1}{\tau}\ln(\frac{C_D(r)}{C_{D+1}(r)}) \tag{3}$$

where τ is the sampling rate of the time series. The formulas converge with increasing D size. In our calculation we show the results for D between 15 and 20.

Supplementary Note 2: Detailed route into and out of chaos

The governing dynamical equations have been described in Ref. [7-9]. In our case, the small modal volume and high Q of photonic crystal (PhC) cavity result in the high intensity of local optical field, optomechanical oscillations [8] and significant two-photon absorption (TPA) effect [7]. Next, TPA mainly produces the heat and free carriers [7, 9]. The dispersion induced by the Kerr effect can be ignored since it is orders of magnitude weaker than the above nonlinearites in silicon [7, 8]. Next, to obtain the main text equations (3) to (6), we

consider the mechanical system is a second-order system (represented by x). With the slowly-varying envelope approximation, the PhC intracavity field is represented by A and the free-carrier density (represented by N) and temperature variation (represented by ΔT) of the PhC cavity is added. One then adds two equations into the equations given in Ref. [7-9], which later become the time-domain nonlinear coupled equations (3) to (6) shown in the main text.

To further illustrate the detailed route into and out of chaos [10-27], a typical sequence of dynamics is given in Supplementary Figure 1. From top to bottom, the injection wavelength detuning is (**a**) 0.910 nm, (**b**) 1.270 nm, (**c**) 1.394 nm, (**d**) 1.831 nm, (**e**) 2.071 nm, (**f**) 2.285 nm, (**g**) 2.406 nm, (**h**) 4.070 nm and (**i**) 5.910 nm respectively. The system is measured both in the frequency-domain (the radio frequency (RF) spectra and in the time-domain (the temporal waveforms and the phase portraits). Based on the unique frequency-temporal characteristics, the dynamical states can be identified. In Supplementary Figure 1, several dynamical states can be identified as: (**a**) the optomechanic oscillation (OMO) state, (**b**) the unstable pulsation state (USP), (**c**) the $f_{omo}/4$ state, (**d**) the $f_{omo}/3$ state, (**e**) the $f_{omo}/2$ state, (**f**) the chaos state (chaos), (**g**) the $f_{omo}/2$ state again, (**h**) the self-induced optical modulation (SOM) state, and (**i**) the stable state (S) respectively. Specifically, for the OMO state, as shown in Supplementary Figure 1a, there is a weak but clear frequency peak shows out at 112MHz. For USP state as shown in Supplementary Figure 1b, the pulses are unstable in both amplitude and period. This is the reason why it is referred to unstable pulses (USP) state. Comparing Supplementary Figure 1b and Supplementary Figure 1c, one can find a resemblance of the temporal waveforms and the phase portraits between the USPs state and $f_{omo}/4$ state. It indicates that the USP state is a transition state into the $f_{omo}/4$ state in PhC-OM system. In brief, the OMO cavity shows rich nonlinear dynamics, following a route of OMO - USP - $f_{omo}/4$ - $f_{omo}/3$ - $f_{omo}/2$ – chaos - $f_{omo}/2$ – SOM - S. Three 2D RF spectral evolution maps of nonlinear and chaotic dynamics, measured with different injection powers, are shown in Supplementary Figure 2(a, b & c). Based on these evolution maps, one can see that the parameter range covered by the various nonlinear dynamical states is gradually increased and extended to the longer wavelength region with increasing the injection power. Furthermore,

we also demonstrate another dynamical route of an optomechanical photonic crystal cavity by scanning the injection power and with the initial low-power detuning Δ fixed at 0.87 nm. In Supplementary Figure 3, from top to bottom, the measured dynamical states follow the sequences of: (**a**) the $f_{omo}/3$ state, (**b**) the chaos state, (**c**) the $f_{omo}/2$ state, (**d**) the SOM state, and finally (**e**) the stable state (pre-OMO state without dynamical fluctuations) S.

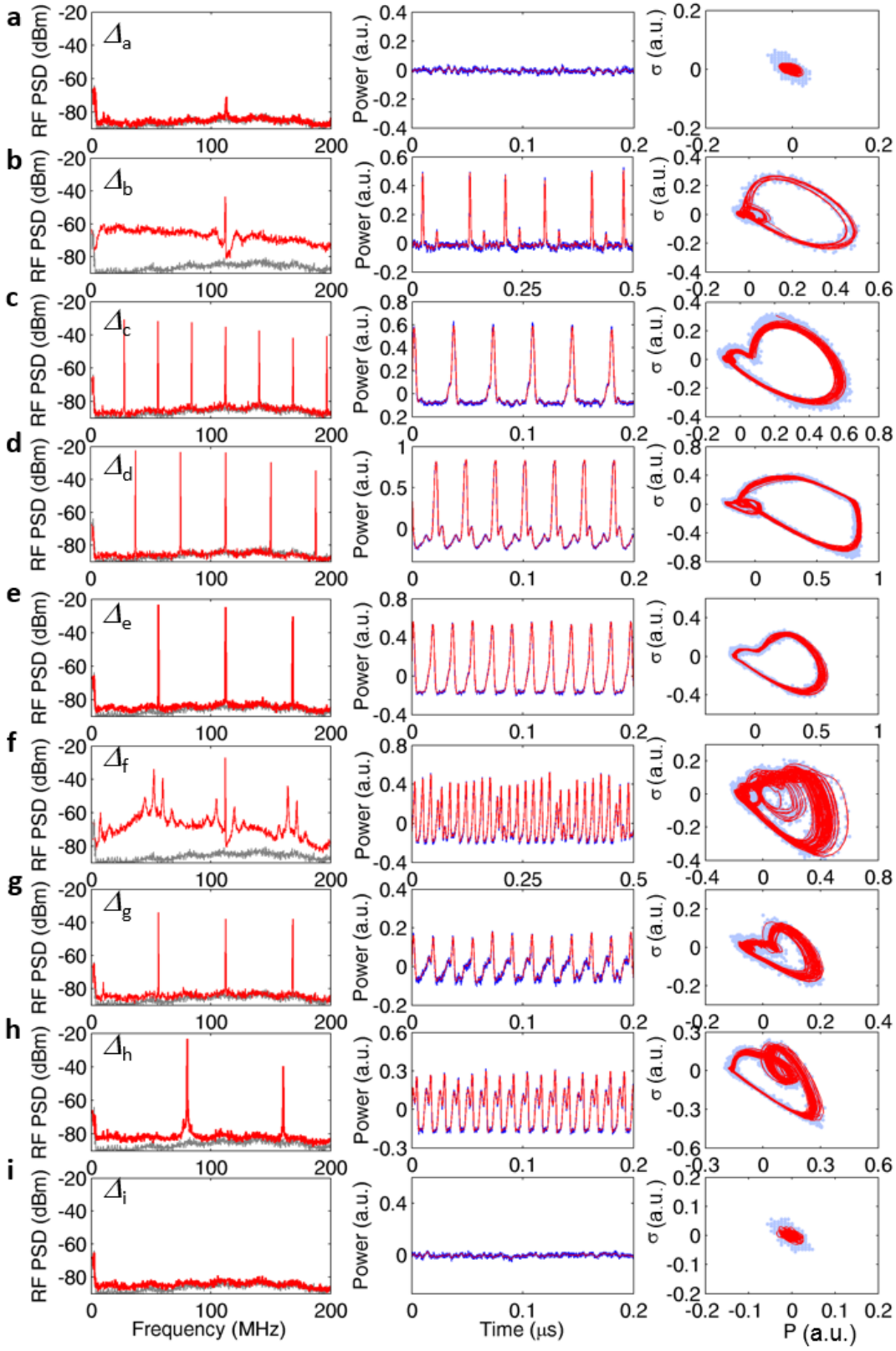

Supplementary Figure 1. **Detailed dynamical transition.** The detuning Δ varies from (**a**) to (**i**) as: (**a**) 0.910 nm, (**b**) 1.270 nm, (**c**) 1.394 nm, (**d**) 1.831 nm, (**e**) 2.071 nm, (**f**) 2.285 nm, (**g**) 2.406 nm, (**h**) 4.070 nm, and (**i**) 5.910 nm respectively. The injection power is kept constant

at 1.26 mW under different injection detuning. The first column shows the measured radio frequency (RF) spectra of different dynamical states, where the grey curves are the background noise floor. The second and third columns show the corresponding temporal waveforms and phase portraits, where the blue dots are the measured data and the solid red curves are the noise-reduced trajectories.

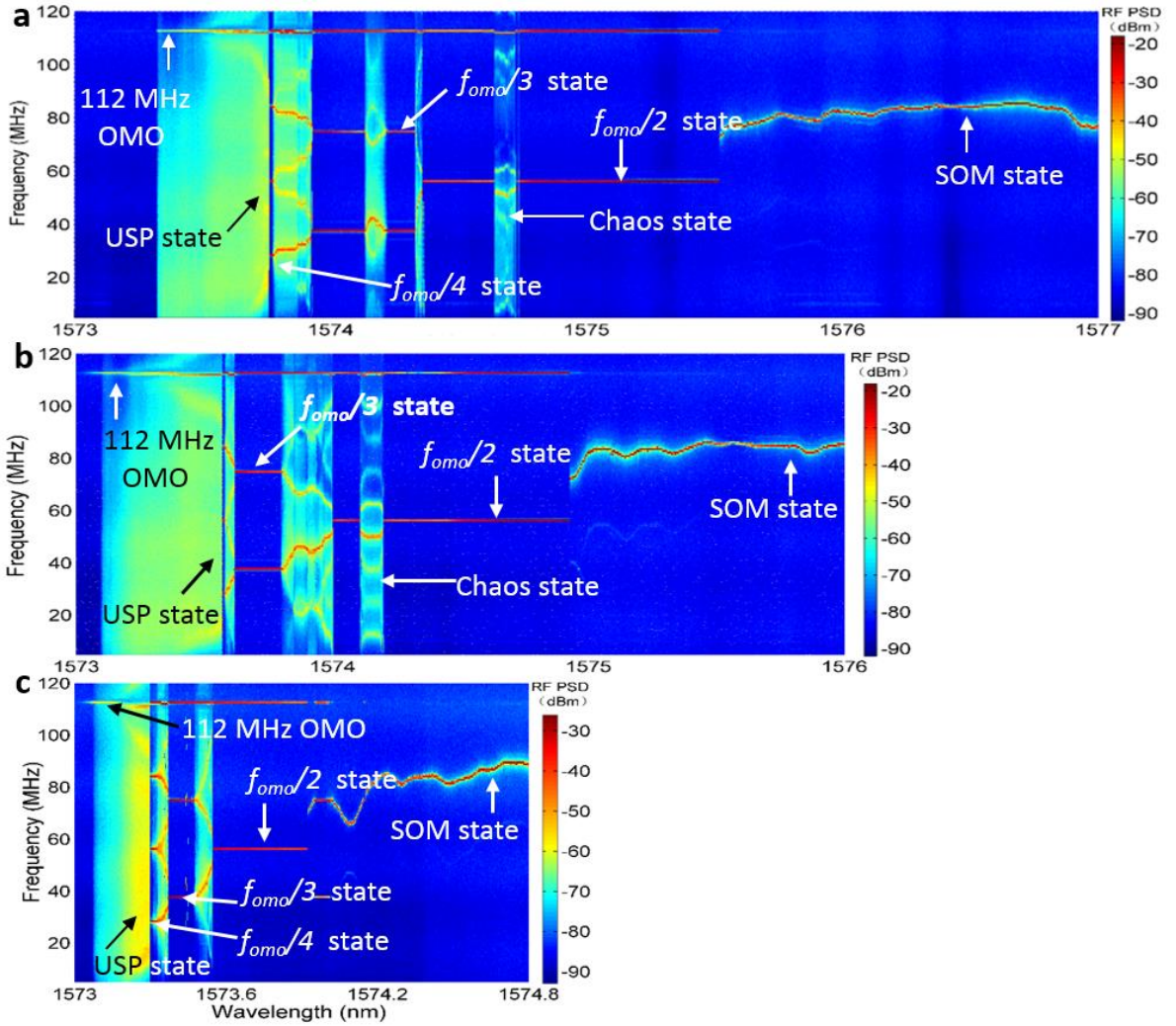

Supplementary Figure 2. **2D RF spectra evolution map of nonlinear dynamics.** The injection power decreases from top to bottom as: (**a**) 0.8 mW, (**b**) 0.5mW, and (**c**) 0.32 mW respectively. The dynamics are detailed as optomechanical oscillation (OMO) state, unstable pulse (USP) state, $f_{omo}/4$ state - $f_{omo}/3$ state, chaos state, $f_{omo}/2$ state and self-induced optical modulation (SOM) state, respectively.

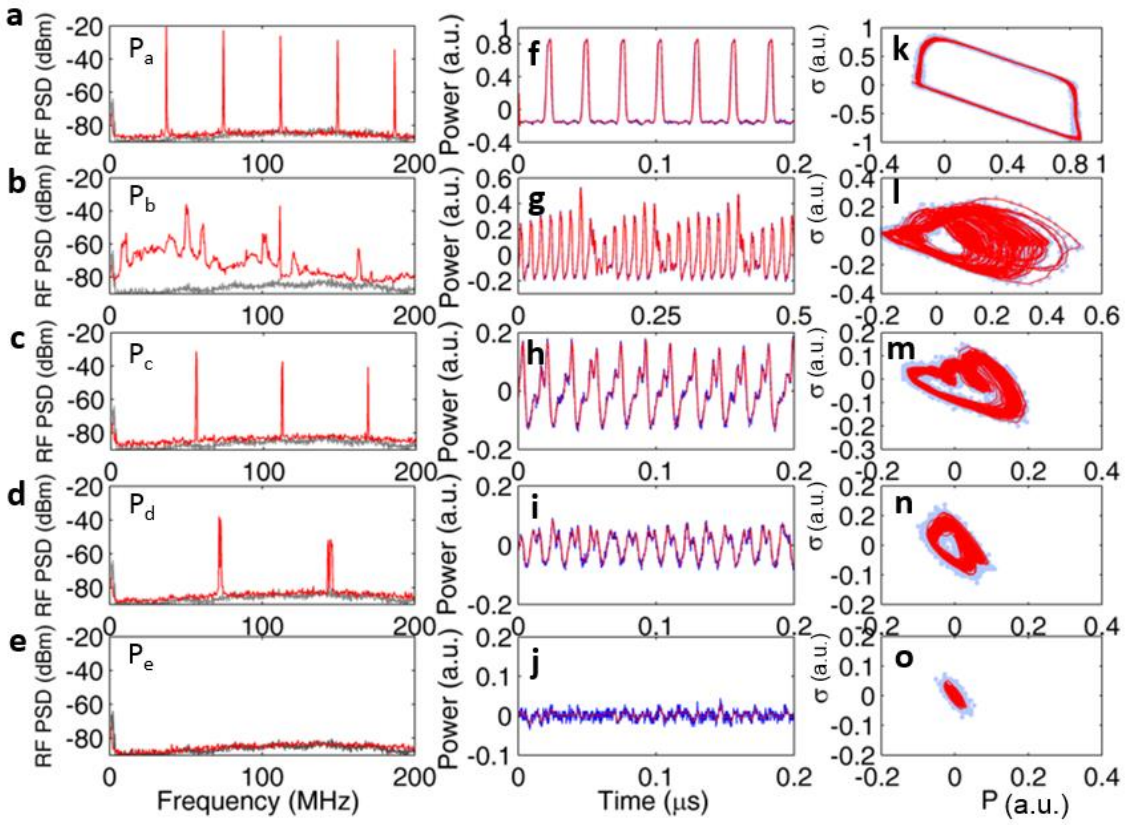

Supplementary Figure 3. **Dynamical evolution under different injection powers.** The injection power increases from top to bottom as: (**a**) 0.68 mW, (**b**) 0.43 mW, (**c**) 0.38 mW, (**d**) 0.22 mW and (**e**) 0.15 mW respectively. The initial low-power detuning Δ is set at 0.87 nm. The (**a**, **b**, **c**, **d** and **e**) shows the measured RF spectra, where the grey curves are the background noise floor. The (**f**, **g**, **h**, **i** and **j**) show the noise-reduced temporal waveforms (red curves), and the (**k**, **l**, **m**, **n** and **o**) show the corresponding phase portraits.

Physically, there are two mechanisms in our slot-type optomechanical PhC chip which consists of the micro-mechanical resonator and the high *Q/V* PhC optical resonator (the detailed coupling scheme is shown in Supplementary Figure 4). Firstly, for a micro-mechanical resonator, with high *Q/V* ratio and sub-wavelength optical confinement, large intracavity radiation pressure forces can modify the motion of micro-mechanical resonators (labeled as ***x*** in equation 3 of the main text) [28, 29]. When the input optical power exceeds the intrinsic mechanical damping losses, a self-sustained oscillation can be formed [29, 30], and is called the OMO limit-cycle from the dynamical point of view. The OMO limit-cycle modulates the PhC optical field (labeled as ***A*** in equation 4 of the main text), and is read out by measuring the optical transmission signal.

Secondly, the high *Q/V* PhC optical resonator is also affected by a series of silicon-based nonlinearities (the nonlinear coupling is shown in Supplementary Figure 4), such as the two-photon absorption (TPA), Drude plasma free-carrier dispersion (FCD), free-carrier absorption (FCA), and the thermo-optic effect [2]. Mainly, the PhC optical mode resonance can be blue-shifted by FCD and red-shifted by the TPA- and FCA-induced thermo-optic effect [7, 8]. This generates a competing relationship between nonlinearities, resulting in a temporal modulation on the PhC optical field. This modulation is called the self-induced optical modulation (SOM) [7, 8]. Next, let us illustrate the SOM process in detail. Initially, a slight red detuning exists between PhC cavity and input laser frequency. A large TPA effect is introduced by the strong optical field in the PhC cavity. TPA generates a large free carrier density (labelled as $\boldsymbol{N}$ in equation 5 of main text). Then, the FCD mechanism and the FCA mechanism will dissipate the free carriers. Firstly, FCD mechanism will cause a rapidly blue-shift of PhC resonance. Secondly, the TPA and FCA will also heats the PhC cavity (labeled as ΔT in equation 6 of the main text), and introduce a slow red-shift of the PhC resonance through the thermo-optic effect. This red-shift will eventually stop the rapid blue-shift, leading to a red-shift of the PhC resonance. Thirdly, eventually the PhC resonance red-shifts over the input laser frequency, and results in a rapid drop of PhC intracavity optical field with a large residual red-shift. Fourthly, the large residual red-shift and thermal energy slowly decays through thermal radiation and thermal conduction of in the silicon structure. Finally, the PhC cavity has cooled and is slightly red-detuned again from the input laser frequency. A SOM type limit-cycle consequently forms. Such SOM limit-cycle will also modulate the PhC optical field. From the dynamical point of view, the OMO limit-cycle and SOM limit-cycle are the degrees of freedom of the PhC optical field. If OMO is absent, the PhC chip will output the periodic SOM signal as shown in Ref. [7, 8]. The coexistence of OMO limit-cycle and SOM limit-cycle adds extra degrees of freedom to the dynamical space of the system and easily destabilizes the dynamics [19, 20, 22]. With effective coupling between OMO and silicon nonlinearities, and enough drive power above the OMO and SOM thresholds, TPA-associated modulations disrupt the OMO rhythm, breaking the OMO limit cycles and creating the non-periodical chaotic oscillations.

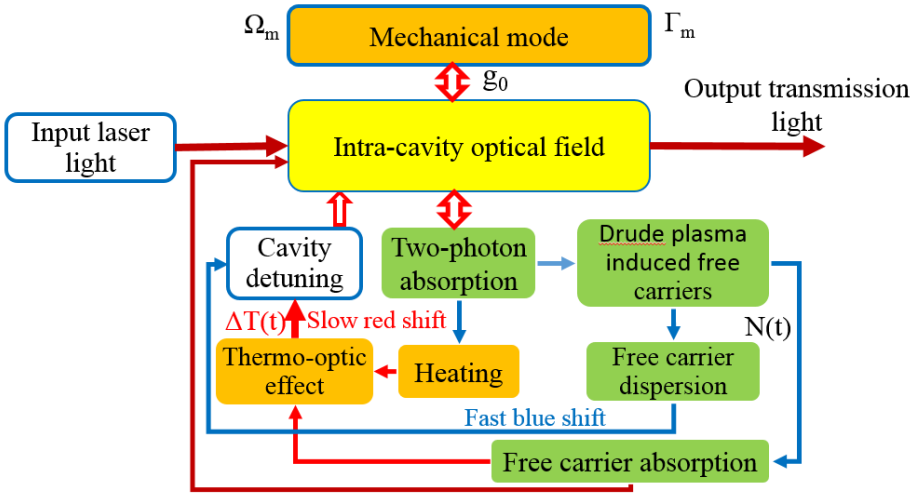

Supplementary Figure 4. **The coupling mechanism of various nonlinearities.** The nonlinearities and mechanical mode of the photonic-crystal optomechanical chip are all considered in our theoretical model [equations (3) to (6) of the main text], where the g_0 is the optomechanics coupling strength, Γ_m is the mechanical dissipation rate, Ω_m is the mechanical angular frequency, ΔT is the cavity temperature variation and N(t) is the free-carrier density. The intracavity optical field is modulated simultaneously both by the mechanical oscillation and by various silicon nonlinearities, such as the two-photon absorption, Drude plasma free-carrier dispersion, free-carrier absorption and the thermo-optic effect. Competitive coupling relationship exists between these nonlinearities, resulting in the complex chaos dynamics.

Supplementary Note 3: Parameters of theoretical modelled and modeled transitional dynamical states

Table 1 summarizes the parameters used in the numerical simulation under the nonlinear coupled mode theory formalism [31, 32]. Material constants are taken from Refs. [7, 8, 33, 34]; other parameters are obtained by measurements, finite-element method (FEM) simulation (COMSOL Multiphysics), and the combination of simulations and experimental fitting. Note that the Kerr nonlinearity and Raman scattering are much weaker than the other nonlinearities and hence they are not included in our model [7, 8, 33, 34].

Supplementary Table 1. **Modelling parameters.**

Parameter	Physical meaning	Value	Source

β_{Si}	Two-photon absorption (TPA) coefficient	8.4×10^{-12} m/W	material constant
n_g	Group index	3.476	material constant
σ_{Si}	Free-carriers absorption (FCA) cross section	1×10^{-21} m^2	material constant
n_{Si}	Refractive index of Si	3.476	material constant
ρ_{Si}	Density of material Si	2.33×10^{3} kg/m^2	material constant
c_p	Specific heat capacity	700 J/(kg K)	material constant
$\frac{dn_{Si}}{dT}$	Thermo-optic coefficient	1.86×10^{-4} K^{-1}	material constant
$\frac{dn_{Si}}{dN}$	Free carrier coefficient	-1.73×10^{-27} m^3	material constant
λ_0	Resonance wavelength	1572.8 nm	measured
γ_i	Linear loss (radiation & abs.)	19 GHz	measured
$\Omega_m/2\pi$	Mechanical frequency	112 MHz	measured
g_0	Vacuum optomechanics (OM)coupling strength	690 kHz	estimated
Γ_{TPA}	TPA confinement factor	0.8012	FEM
V_{TPA}	TPA mode volume	6.4×10^{-19} m^3	FEM
m_{eff}	Mechanical osc. effective mass	2.4×10^{-14} kg	FEM
Γ_{FCA}	FCA confinement factor	0.79	FEM
V_{FCA}	FCA mode volume	6.9×10^{-19} m^3	FEM
Γ_{PhC}	Thermal confinement factor	0.769	FEM
τ_{fc}	Free-carrier lifetime	150 ps	fitted
τ_{th}	Thermal dissipation life time	9.7 ns	fitted
$\Gamma_m/2\pi$	Mechanical dissipation rate	110 kHz	estimated

$\gamma_e/2\pi$	External coupling rate	2.2 GHz	estimated
V_{PhC}	Thermal mode volume	1×10^{-18} m^3	estimated

Supplementary Figure 5 shows an example of the simulated chaos and the associated dynamical transitions of the two-photon optomechanical photonic crystal cavity. Supplementary Figure 5a shows the pure OMO state. Next, Supplementary Figure 5b, 5c, 5d show the $f_{omo}/2$ state, $f_{omo}/3$ state and $f_{omo}/4$ state respectively. Clear sub-harmonic frequency peaks can be observed in these Fourier transformed power spectra, and the corresponding phase portraits also characterize clearly the limit-cycle features. Supplementary Figure 5e gives the simulated chaotic oscillation; its power spectrum distributes continuously, being quite different from the discrete distribution spectrum. The temporal waveform (Supplementary Figure 5j) behaves intricately. Moreover, the corresponding phase orbit (Supplementary Figure 5o) consistently winds and stretches in the basin of the strange attractor; this induces the fractal structure [2, 6, 35]. These simulations confirm qualitatively the experimental observations of Figure 2 in the main text. In addition, we emphasize that the obtained chaos is deterministic since the simulation equations (3)-(6) are deterministic and do not contain any noise terms.

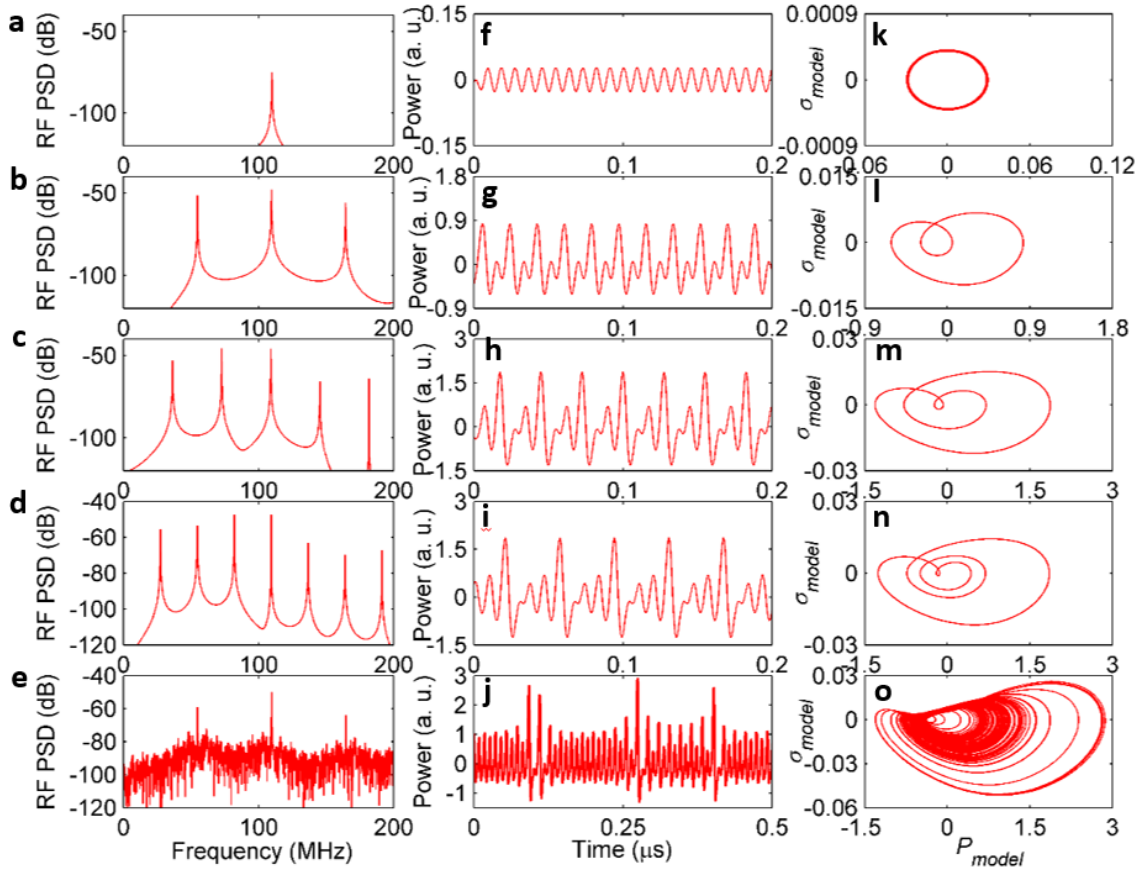

Supplementary Figure 5. **Numerical simulations of chaotic output.** (**a-e**): Fourier transformed power spectrum. (**f-j**): temporal waveform. (**k-o**): corresponding phase portrait, where the injection power P_{in} is 1 mW and normalized detuning $\delta\omega$ /γ_i varies from top to bottom as: (**a, f, k**) 2, (**b, g, i**) 5.5, (**c, h, m**) 8.65, (**d, i, n**) 7.95, and (**e, j, o**) 10. The mechanical frequency $\Omega_m/2\pi$ value is 110 MHz and other parameters are given in Supplementary Table 1.

Supplementary Note 4: Effects of the optomechanics coupling strength g_0 in chaotic transition and routes

The large optomechanical (OM) coupling strength (g_0) means the strong coupling between optical field and mechanical motion in the PhC nanocavity. The localized mode of the PhC-OM cavity has a much larger g_0 than regular large Fabry-Perot cavities. The OM coupling strength (g_0) is estimated using the phase modulation method described in [36, 37]:

$$g_0^2 \approx \frac{1}{2\overline{n}_{th}} \frac{\Phi_0^2 \Omega_{mod}^2}{2} \frac{S(\Omega_m) \times \Gamma_m/4}{S(\Omega_{mod}) \times RBW} \qquad (4)$$

where $\overline{n}$ is the average phonon occupancy, ϕ_0 is the phase modulation amplitude, and Ω_{mod} is

the modulation angular frequency. The proportion between $S(\Omega_m)$ and $S(\Omega_{mod})$ is obtained by measuring the peak spectral power of the mechanical oscillation and that of phase modulation signals. RBW is the resolution bandwidth of the spectrum analyzer, and $\Gamma_m/2\pi$ is the dissipation rate of the mechanical oscillator. For the chip used in this manuscript, the value of g_0 is determined to be about 690 kHz.

To further illustrate the effect of the coupling strength g_o on the chaos generation, we examine theoretically a varied coupling strength g_o between the OMO and photonic crystal cavity nonlinearities based on the numerical model. The coupling between resonators usually leads to the generation of complex nonlinear dynamics [38-40]. Supplementary Figure 6 shows the simulated dynamical evolution under different g_o values. First, the system has pure OMO transmission signal for a small coupling strength g_o. Next, when g_o grows over a specific value (about 330 kHz), discrete frequency components can be observed at the locations of multiples of $f_{omo}/2$ or $f_{omo}/4$. It means the system has evolved into the $f_{omo}/2$ or $f_{omo}/4$ states. Along with the increase of g_o value, the OMO couples strongly with cavity nonlinearities. When g_0 grows over a threshold value (about 670 kHz), the system shows complex evolution and finally transits into the chaos state. Thus, sufficiently strong g_o is a necessary condition for the chaos generation. In addition, it should be noted the threshold g_o value is dependent on the varied injection conditions, such as the injection power and detuning. A theoretical analysis has been addressed for the physical reasons of this deviation from eigenmode mechanical oscillations [41]. This is the reason why the chaos state only appears at specific ranges of injection detunings and powers as shown experimentally in Figure 4, Supplementary Figures 1 & 3.

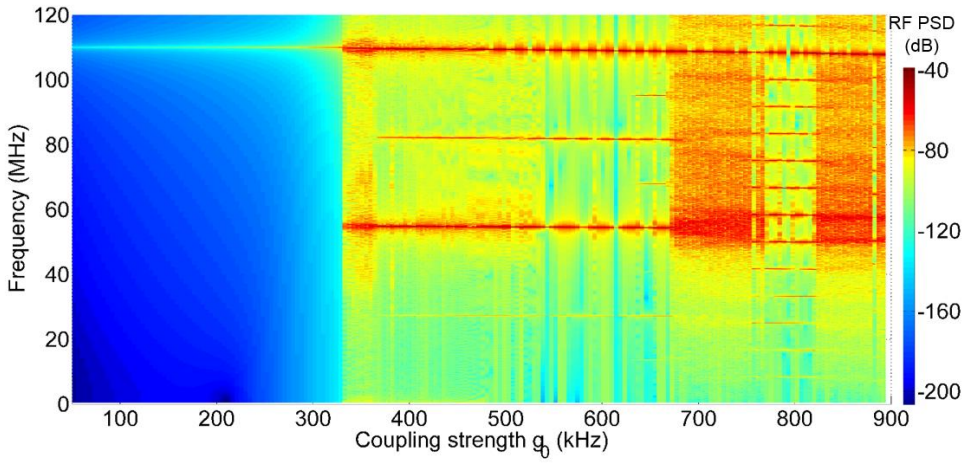

Supplementary Figure 6. **Investigation of dynamics evolution under different value of g_0.** Simulated 2D radio frequency (RF) spectral map with varied dynamics for different coupling strength g_0 values, with the injection power fixed at P_{in} = 1 mW and the normalized detuning at 10. The mechanical frequency $\Omega_m/2\pi$ value is 110 MHz and the other parameters are given in Supplementary Table 1. The inset shows the fine evolution of the RF frequency around 110 MHz, with the slight RF frequency shift from increased g_0 and stronger optical gradient force.

Supplementary Note 5: Effects of the laser-cavity detuning in chaotic transition and routes

Supplementary Figure 7 illustrates the simulated 2D RF spectral map with dynamics evolution under different detunings $\delta\omega/\gamma_i$, with the injection power P_{in} at 1.26 mW. In the Supplementary Figure 7, the left regime is the OMO state in the range of $\delta\omega/\gamma_i$ less than 3.5. The pure OMO signal is present at 112 MHz. Second, in the range of $3.5 < \delta\omega/\gamma_i < 8.5$, the USP state appears. The identification of the USP state could be carried out by combining the spectral feature and the temporal characteristics together. The spectral distribution of the USP state is continuous, but the temporal waveform of the USP state is irregular pulsing, as shown in Supplementary Figure 1b. Furthermore, complex high-order harmonics are also interspersed among the USP region. Third, the $f_{omo}/3$ state appears in a small window at $\delta\omega/\gamma_i \approx 8.5$. In addition, the $f_{omo}/2$ state appears in the range of $\delta\omega/\gamma_i \approx 10$. Significant $f_{omo}/2$ components appear in the RF spectra but have associated relatively weak $f_{omo}/4$ components. Next, the system evolves into the chaos state in the range $\delta\omega/\gamma_i \approx 11$. As shown by the RF

spectra, the chaos evolution is dominated by both the OMO and the SOM together, indicating the chaos comes from the coupling between the OMO and SOM oscillation. Finally, for $\delta\omega/\gamma_i$ greater than 12, the SOM state becomes the dominant dynamics while the OMO oscillation disappears. Overall, the above numerical results predict a dynamical transition to chaos of OMO - USP - $f_{omo}/3$ - $f_{omo}/2$ - chaos - SOM as a function of detuning. This modeled dynamics evolution is in qualitative agreement with the experimental observations in Figure 1d.

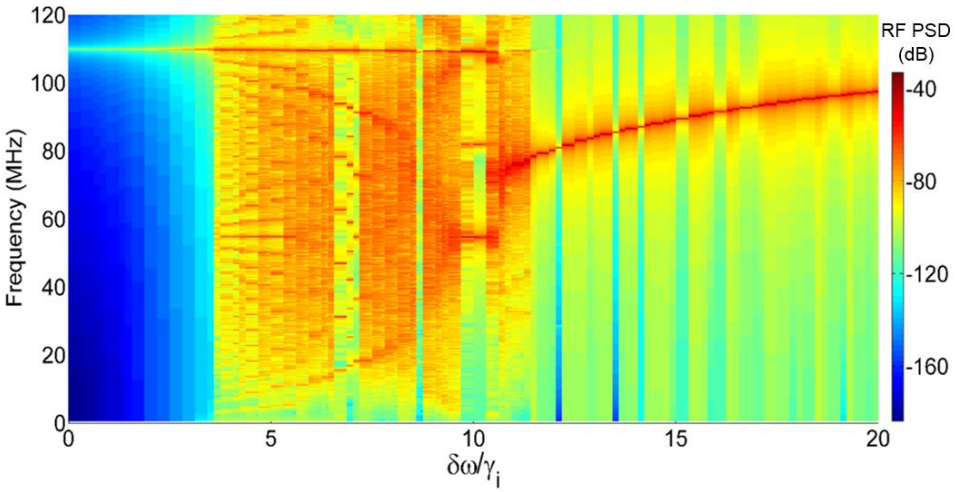

Supplementary Figure 7. **The dynamics evolution under different detunings.** Simulated 2D radio frequency (RF) spectral map with various dynamics under normalized laser-cavity detunings from 0 to 20, with the injection power P_{in} = 1.26 mW and optomechanical coupling strength g_0 = 690 kHz. The other parameters are shown in Supplementary Table 1.

Supplementary Note 6: Co-located two-photon-induced Drude free-carrier plasma and optomechanical dynamics

To investigate the coupling between the OMO and silicon nonlinearities, we separate artificially the OMO and silicon nonlinearities [8, 28-30, 36, 42] in our numerical simulations, and then recombine them together again. First, we get a simplified OM oscillator by setting all photonic crystal cavity nonlinear coefficients to zero, as Γ_{TPA} = 0, Γ_{FCA} = 0, Γ_{phc} = 0, dn_{Si}/dT = 0 and dn_{Si}/dN = 0, respectively. Supplementary Figure 8a shows the corresponding OMO evolution under different injection powers and the normalized detuning fixed at 10. It shows that no complex nonlinear dynamics are observed, and the pure OMO is present at the intrinsic 110 MHz frequency and with a monotonic increase in RF power with increasing

injection power. Second, by setting g_o at 0 (without OMO), we numerically obtain a purely photonic crystal cavity regenerative modulation. Supplementary Figure 8b shows the cavity dynamical evolution under different injection powers. It can be seen that there is no observable self-induced optical modulation (SOM) [7, 8] in the relatively low P_{in} condition for $P_{in} < 1.56$ mW. For P_{in} larger than 1.56 mW, the SOM and its harmonics emerge at the frequency 66 MHz and 132 MHz, and gradually decrease along with the increase of P_{in} due to the larger thermal effects and longer relaxation time to the periodic origin state. It should be noted that the 66 MHz SOM is comparable with the half of OMO frequency $f_{omo}/2$ at 55 MHz, supporting the occurrence of the $f_{omo}/2$ state.

Third, Supplementary Figure 8c shows the dynamical evolution of the optomechanical cavity system when combining the OMO and the photonic crystal Drude electron-hole plasma nonlinearities together. The chaos state is present at the broad area of the medium P_{in} condition (labelled region *II* for $1.56 < P_{in} < 2.18$ mW), originating from the large coupling between OMO and SOM. For higher P_{in} condition (labelled region *III* for $P_{in} > 2.18$ mW), discrete frequency components are present at multiples of $f_{omo}/2$, demonstrating the $f_{omo}/2$ state. Generally, in a system that has two intrinsic frequencies, harmonic frequency locking will occur when the frequency ratio is close to a rational value [43, 44]. For example, in our PhC-OM chip, the frequency SOM is about 60 MHz for $P_{in} > 2.18$ mW, reasonably close to the $f_{omo}/2$. Consequently, the 1/2-harmonic locking occurs, and discrete frequency with integer multiple $f_{omo}/2$ is present in the theoretical simulations (labelled region *III* in Supplementary Figure 8c] and experimental observations (shown in Supplementary Figure 3c). Since the SOM frequency varies with the change of driving conditions, other orders of frequency locking and different OMO sub-harmonic states can also be observed experimentally [Supplementary Figure 1 & 3] and theoretically [Supplementary Figure 5, 7 & 8c].

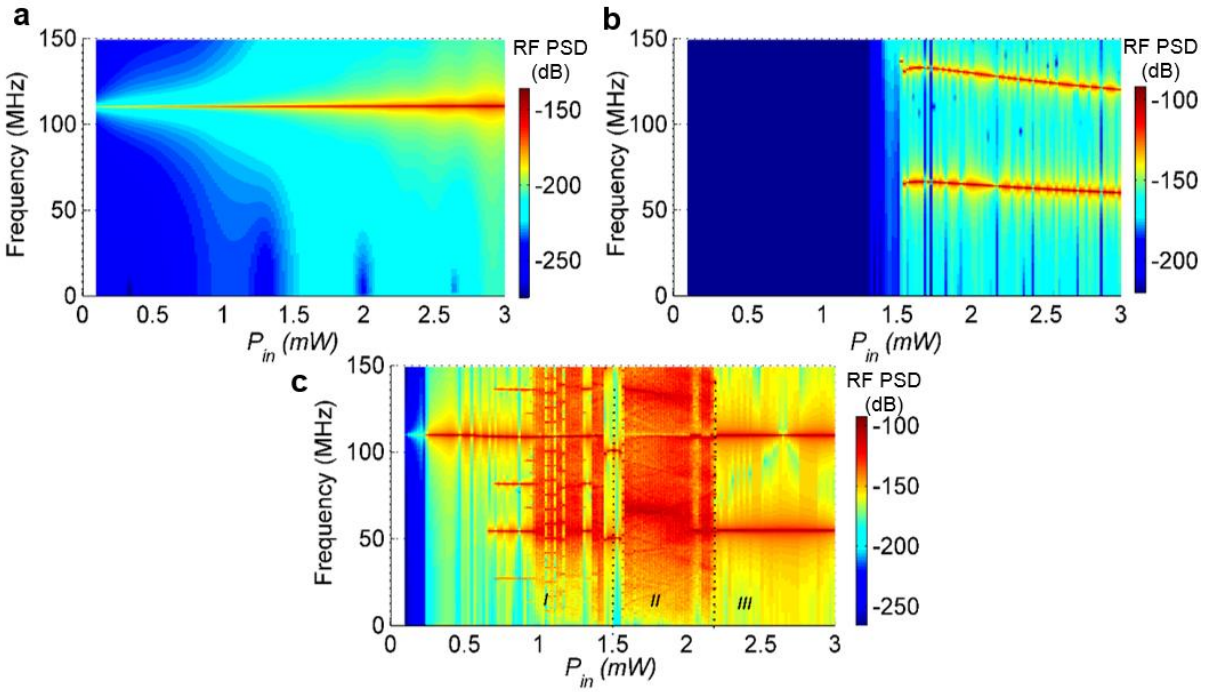

Supplementary Figure 8. **Investigations of the coupling between OMO and plasma.** (**a**), Modelled optomechanical oscillation (OMO) evolution under varying injection powers P_{in} without any photonic crystal cavity nonlinearities. (**b**), Modelled cavity evolution under varying injection powers P_{in} with cavity nonlinearity but without optomechanical mechanism by setting g_0 to 0. (**c**), Dynamical evolution of the recombined optomechanical photonic crystal cavity system under varying injection powers P_{in}, with g_0= 690 kHz and the cavity nonlinearity values shown in Supplementary Table 1. The three dynamical regions are labelled '*I*' (for $P_{in} < 1.56$ mW), '*II*' (for $1.56 < P_{in} < 2.18$ mW) and '*III*' (for $P_{in} > 2.18$ mW), respectively.

Supplementary Note 7: Effects of the intracavity energy and drive power

Supplementary Figure 9a further illustrates the evolution curves of the OMO frequency and the two-photon-induced SOM frequency under different injection powers. Combining the dynamical evolution presented in Supplementary Figure 8c, there are three dynamical regions: *I* labels the bifurcation transition routes from pure OMO to $f_{omo}/2$, $f_{omo}/4$, then into the chaos region; *II* labels the chaos region; and *III* labels the $f_{omo}/2$ region. Firstly, in region *II*, the OMO couples strongly with SOM. The oscillation rhythm is disrupted and leads to the intricate chaotic states. In region *III*, the SOM frequency decreases to close to half of the OMO frequency. Meanwhile, the OMO becomes much stronger than that of region *I* and of region *II* according to the Supplementary Figure 8a. Then, frequency locking happens between OMO and SOM, and $f_{omo}/2$ is formed. Third, in the region *I*, there is no apparent SOM as illustrated in Supplementary Figure 8b. But in Supplementary Figure 8c, the system is unstable with a series of bifurcations and evolves gradually into the chaos state. As seen in Supplementary Figure 9b & 9c, one could find that the P_{in} already stimulates considerable N and ΔT in the region *I* in optomechanical photonic crystal cavity when the intracavity mode energy $|A|^2$ is relatively low as shown in Supplementary Figure 9d. These N and ΔT increase constantly along with the increase of P_{in}, also significantly destabilizing the OMO, and then leads to the bifurcation of the $f_{omo}/2$ state, $f_{omo}/4$ state, and even the chaos state. The above results illustrate that the large coupling between OMO and photonic crystal nonlinearities is key for the chaos generation.

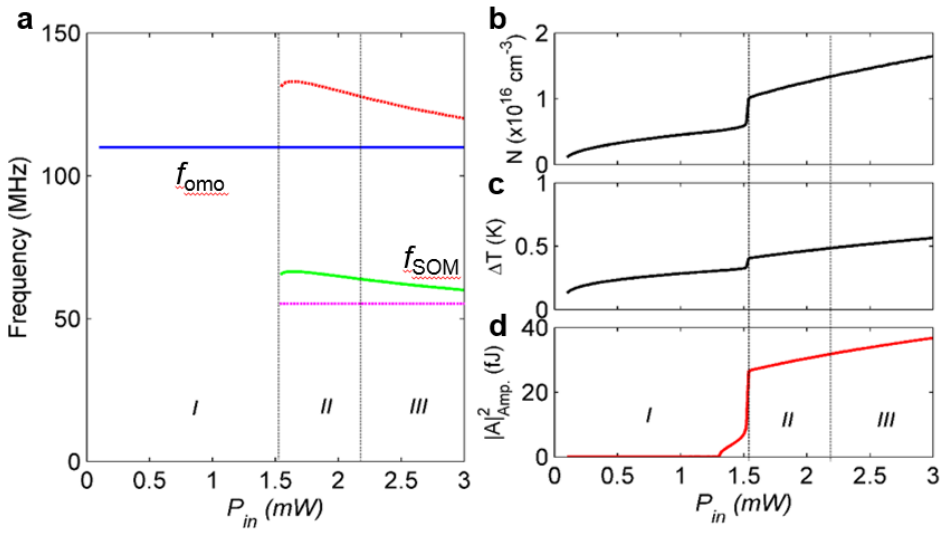

Supplementary Figure 9. **Evolution of the OMO, SOM and the PhC nonlinearities.** (**a**), Evolution of OMO frequency f_{omo} (blue line) and SOM frequency f_{SOM} (green line) and $f_{omo}/2$ (purple dot line) and 2nd harmonics of f_{SOM} (red dot line) under varying injection powers P_{in}. (**b**) Corresponding evolution of intracavity free carrier density N. (**c**) Evolution of intracavity temperature variation ΔT. (**d**) Evolution of the amplification of the intracavity mode energy $|A|^2$. The three regions are labelled as '*I*' (for $P_{in} < 1.56$ mW), '*II*' (for $1.56 < P_{in} < 2.18$ mW) and '*III*' (for $P_{in} > 2.18$ mW), respectively.

Supplementary References

1. Schreiber, T. Determination of the noise level of chaotic time series. *Phys. Rev. E* **48**, R13-R16 (1993).
2. Sprott J. C. *Chaos and Time Series Analysis* (Oxford University Press, 2003).
3. Brown, R., Bryant, P. & Abarbanel H. D. I. Computing the Lyapunov spectrum of a dynamical system from an observed time series. *Phys. Rev. A* **43**, 2787-2806 (1991).
4. Grassberger, P., & Procaccia, I. Characterization of strange attractors. *Phys. Rev. Lett.* **50**, 346-349 (1983).
5. Grassberger, P., & Procaccia, I. Estimation of the Kolmogorov entropy from a chaotic signal. *Phys. Rev. A* **28**, 2591-2593 (1983).
6. Grassberger, P., & Procaccia, I. Measuring the strangeness of strange attractors. *Physica D* **9**, 189-208 (1983).
7. Johnson, T. J., Borselli, M. & Painter, O. Self-induced optical modulation of the transmission through a high-*Q* silicon microdisk resonator. *Opt. Express* **14**, 817-831 (2006).
8. Aspelmeyer, M., Kippenberg, T. J. & Marquardt F. Cavity optomechanics. *Rev. Mod. Phys.* **86**, 1391-1452 (2014).
9. Yang, J. *et al.* Radio frequency regenerative oscillations in monolithic high-*Q/V* heterostructured photonic crystal cavities. *Appl. Phys. Lett.* **104**, 061104 (2014).
10. Li, T.-Y., & Yorke, J. A. Period three implies chaos. *The American Mathematical Monthly* **82**, 985-992 (1975).
11. Lorenz, E. N. Deterministic nonperiodic flow. *J. Atmos. Sci.* **20**, 130-141 (1963).
12. Haken, H. Analogy between higher instabilities in fluids and lasers. *Phys. Lett. A* **53**, 77-78 (1975).
13. Teitsworth, S. W., Westervelt, R. M., & Haller, E. E. Nonlinear oscillations and chaos in electrical breakdown in Ge. *Phys. Rev. Lett.* **51**, 825-828 (1983).
14. Held, G. A., Jeffries, C., & Haller, E. E. Observation of chaotic behavior in an electron-hole plasma in Ge. *Phys. Rev. Lett.* **52**, 1037-1080 (1984).
15. Gwinn, E. G., & Westervelt, R. M. Frequency locking, quasiperiodicity, and chaos in extrinsic Ge. *Phys. Rev. Lett.* **57**, 1060-1063 (1986).
16. Pecora, L. M., & Carroll, T. L. Synchronization in chaotic systems. *Phys. Rev. Lett.* **64**, 821-824 (1990).

17. Garcia-Ojalvo, J. & Roy, R. Spatiotemporal communication with synchronized optical chaos. *Phys. Rev. Lett.* **86**, 5204-5207 (2001).
18. VanWiggeren, G. D. & Roy, R. Communication with chaotic lasers. *Science* **279**, 1198-1200 (1998).
19. Poincaré, H. *Science and Method* (Courier Dover Publications, 2013).
20. Chen, Y. C., Winful, H. G. & Liu, J.-M. Subharmonic bifurcations and irregular pulsing behavior of modulated semiconductor lasers. *Appl. Phys. Lett.* **47**, 208-210 (1985).
21. Schreiber, T. Determination of the noise level of chaotic time series. *Phys. Rev. E* **48**, R13-R16 (1993)
22. Coffey, D. S. Self-organization, complexity and chaos: the new biology for medicine. *Nat. Med.* **4**, 882-885 (1998).
23. Peitgen, H.-O., Jürgens, H., Saupe, D. *Chaos and fractals: new frontiers of science* (Springer, 2004).
24. Zheng, J. *et al.* Feedback and harmonic locking of slot-type optomechanical oscillators to external low-noise reference clocks. *Appl. Phys. Lett.* **102**, 141117 (2013).
25. Sun, Y., & Sukhorukov, A. A. Chaotic oscillations of coupled nanobeam cavities with tailored optomechanical potentials. *Opt. Lett.* **39**, 3543-3546 (2014).
26. Ma, J. *et al.*Formation and manipulation of optomechanical chaos via a bichromatic driving. *Phys. Rev. A* **90**, 043839 (2014).
27. Sciamanna M. & Shore. K. A., Physics and applications of laser diode chaos, *Nature Photon.* **9**, 151-162 (2015).
28. Thompson, J. D. *et al.* Strong dispersive coupling of a high-finesse cavity to a micromechanical membrane. *Nature* **452**, 72-75 (2008).
29. Carmon, T., Rokhsari, H., Yang, L., Kippenberg, T. J. & Vahala, K. J. Temporal behavior of radiation-pressure-induced vibrations of an optical microcavity phonon mode. *Phys. Rev. Lett.* **94**, 223902 (2005).
30. Kippenberg, T. J., Rokhsari, H., Carmon, T., Scherer, A. & Vahala K. J. Analysis of radiation-pressure induced mechanical oscillation of an optical microcavity. *Phys. Rev. Lett.* **95**, 033901 (2005).
31. Haus, H. A., *Waves and fields in optoelectronics* (Prentice-Hall, 1984).
32. Yang, X. & Wong, C. W., Coupled-mode theory for stimulated Raman scattering in high-Q/V_m silicon photonic band gap defect cavity lasers. *Opt. Express* **15**, 4763-4780 (2007).
33. Hossein-Zadeh, M., & Vahala K. J. An optomechanical oscillator on a silicon chip. *IEEE J. Sel. Top. in Quant. Elect.* **16**, 276-287 (2010).
34. Abrams, D. M., Slawik, A. & Srinivasan K. Nonlinear oscillations and bifurcations in silicon photonic microresonators. *Phys. Rev. Lett.* **112**, 123901 (2014).
35. Ott, E. *Chaos in Dynamical Systems* (Cambridge University Press, 2002).
S36. Gavartin, E. *et al.* Optomechanical coupling in a two-dimensional photonic crystal defect cavity. *Phys. Rev. Lett.* **106**, 203902 (2011).
S37. Luan, X. *et al.* An integrated low phase noise radiation-pressure-driven optomechanical oscillator chipset. *Sci. Rep.* **4**, 6842 (2014).

S38. Buskirk, R. V., & Jeffries C. Observation of chaotic dynamics of coupled nonlinear oscillators. *Phys. Rev. A* **31**, 3332-3357 (1985).
S39. Karabalin, R. B., Cross, M. C. & Roukes M. L. Nonlinear dynamics and chaos in two coupled nanomechanical resonators. *Phys. Rev. B* **79**, 165309 (2009).
S40. Mancinelli, M., Borghi, M., Ramiro-Manzano, F., Fedeli, J. M. & Pavesi L. Chaotic dynamics in coupled resonator sequences. *Opt. Express* **22**, 14505-14516 (2014).
S41. Wurl, C., Alvermann, A. & Fehske H. Symmetry breaking oscillations in membrane optomechanics. arXiv:1609.05645v1.
S42. Akahane, Y., Asano, T., Song, B.-S. & Noda S. High-*Q* photonic nanocavity in a two-dimensional photonic crystal. *Nature* **425**, 944-947 (2003).
S43. Gilbert T. & Gammon, R. Stable oscillations and Devil's staircase in the Van der Pol oscillator. *Int. J. Bifurcation Chaos* **10**, 155-164 (2000).
S44. Lin F. Y. & Liu, J. M. Harmonic frequency locking in a semiconductor laser with delayed negative optoelectronic feedback. *Appl. Phys. Lett.* **81**, 3128-3130 (2002).